Unconventional charge density wave in a kagome lattice antiferromagnet FeGe

Xikai Wen,[1] Yuqing Zhang,[1] Chenglin Li,[6,7] Zhigang Gui,[1] Yikang Li,[2] Yanjun Li,[1] Xueliang Wu,[3] Aifeng Wang,[3] Pengtao Yang,[6] Bosen Wang,[6] Jinguang Cheng,[6] Yilin Wang,[2,4,*] Jianjun Ying,[1,4,†] and Xianhui Chen[1,2,4,5,‡]

[1]*Department of Physics, and CAS Key Laboratory of Strongly Coupled Quantum Matter Physics, University of Science and Technology of China, Hefei, Anhui 230026, China*

[2]*Hefei National Research Center for Interdisciplinary Sciences at the Microscale, University of Science and Technology of China, Hefei 230026, China*

[3]*Low Temperature Physics Laboratory, College of Physics and Center of Quantum Materials and Devices, Chongqing University, Chongqing 401331, China*

[4]*Hefei National Laboratory, Hefei 230088, China*

[5]*Collaborative Innovation Center of Advanced Microstructures, Nanjing University, Nanjing, 210093, China*

[6]*Beijing National Laboratory for Condensed Matter Physics and Institute of Physics, Chinese Academy of Sciences, Beijing 100190, China*

[7]*School of Physical Sciences, University of Chinese Academy of Sciences, Beijing 100190, China*

(Received 18 January 2024; accepted 7 August 2024; published 27 August 2024)

FeGe is a kagome material that exhibits both charge density wave (CDW) order and magnetic order. The CDW order is developed deep inside the *A*-type antiferromagnetic phase in FeGe, providing a unique platform to investigate the interplay between CDW and magnetism. However, the driving mechanism of the CDW phase remains controversial. In this work, we performed high-pressure electrical transport and x-ray diffraction measurements combined with density-functional theory calculations to investigate the evolution of the CDW of FeGe under pressure. In contrast to conventional CDW materials, the CDW transition temperature of FeGe increases with increasing pressure, indicating the unconventional mechanism of CDW in this material. More interestingly, another possible CDW with a $\sqrt{3} \times \sqrt{3} \times 6$ superlattice emerges above 20 GPa, which may be explained by the calculated metastable CDW states under high pressure. These observations exclude the possibility of Van Hove singularities nesting as a CDW driving force. Our results unveil versatile CDW states and broaden the study of intertwined electronic states in the magnetic kagome metal FeGe.

DOI: 10.1103/PhysRevResearch.6.033222

I. INTRODUCTION

The corner-shared triangle network geometric characteristics of the two-dimensional (2D) kagome lattice can give rise to a unique electronic band structure, including a dispersionless flat band originating from destructive phase interference, a topological Dirac band around the *K* point, and a pair of Van Hove singularities (VHSs) with logarithmic divergence located at the *M* point [1–12]. Rich emergent electronic states can be realized at select band fillings [1–15]. The flat bands possess high densities of states, which dramatically enhance the correlation effects between electrons so that magnetic order [1–3] can emerge when the flat bands are located near the Fermi level. When the energy band is filled in the vicinity of the VHSs, the divergent DOS is preeminently suited for the emergence of novel Fermi surface instabilities and induces a charge density wave (CDW) [4–8], spin density wave (SDW) [6], and chiral superconductivity [6,7,13] with singular behavior. Moreover, the gapped-out Dirac points confer energy band nontrivial topological properties [11,14,15].

The kagome materials AV_3Sb_5 (A = K, Rb, Cs) have attracted tremendous attention due to the observation of nontrivial band topology, unconventional charge density wave (CDW) order, and superconductivity (SC) [16–33]. Time-reversal symmetry breaking [23,27,34] as well as a giant anomalous Hall effect [28,35] were observed in the CDW state without long-range magnetic order, which was associated with a possible chiral flux phase [21,23,36]. Further high-pressure studies revealed unconventional competition between CDW and superconductivity in CsV_3Sb_5 [37,38], broadening the understanding of the intertwined electronic states. However, the absence of magnetic order in the weakly electron-correlated AV_3Sb_5 family limits the understanding of the interplay between CDW and magnetism. The emergent CDW in magnetic kagome metal FeGe filled the gap in this regard. B35-type FeGe is a strongly electron-correlated kagome magnet [39]. It exhibits collinear *A*-type antiferromagnetic (AFM) order below the Néel temperature $T_N \sim 410$ K [40] and becomes a *c*-axis double-cone AFM structure below a lower transition temperature $T_{Canting} \sim 60$ K [41–46].

*Contact author: yilinwang@ustc.edu.cn
†Contact author: yingjj@ustc.edu.cn
‡Contact author: chenxh@ustc.edu.cn

The CDW order was observed deep inside the *A*-type AFM phase [39,47–49] around $T_{CDW} \sim 110$ K in FeGe. The emergent anomalous Hall effect and significantly enhanced AFM ordered moment were observed below T_{CDW}, suggesting a strong coupling between the CDW and AFM order [47]. However, the driving mechanism of the CDW phase and the interplay between CDW and magnetism remain controversial [39,49–54]. Previous angle-resolved photoemission spectroscopy (ARPES) measurements found that magnetic exchange splitting pushes orbital-dependent VHSs near the Fermi level and proposed that CDW order is driven by nesting among VHSs [39,47]. However, the absence of CDW order in other *A*-type AFM kagome systems such as FeSn [9] suggests a limitation of this scenario. Density-functional theory (DFT) calculations also indicate that VHSs are close to the Fermi surface only in a small k_z range, which is not dominant in the nesting function [51]. In addition, the absence of a negative phonon branch indicates that structural distortions due to CDW phase transition will not occur in FeGe [49,51]. Recent theoretical calculations show that the energetically favored $2 \times 2 \times 2$ superstructure in FeGe is stabilized by strong spin-phonon interactions [49,53]. This behavior is very different from the nonmagnetic kagome family AV_3Sb_5, in which VHSs nesting play an essential role in the CDW transition and an imaginary phonon appears around the *M* point [18,22,23,27,36], indicating an unconventional mechanism in stabilizing CDW in FeGe. These contradictions hinder the understanding of the mechanism of CDW formation in the magnetic kagome metal FeGe, which needs urgent clarification using further experiments.

In this work, we performed high-pressure electrical transport measurements on FeGe single crystals and found that the CDW transition temperature unexpectedly increases with increasing pressure, consistent with the decrease in the total energies of the CDW state with increasing pressure obtained from DFT+*U* calculations based on large dimerization of Ge1 sites. In addition, the calculated band structures show that the VHS at the *M* point is further pushed away from the Fermi level under pressure, which excludes the possibility of the nesting of VHSs as the CDW driver in FeGe. More interestingly, another possible CDW with a $\sqrt{3} \times \sqrt{3} \times 6$ superlattice emerges above 20 GPa, which may be explained by the calculated metastable CDW states under high pressure. Our results exclude the possibility of VHSs nesting as a CDW driving force, and support the scenario that a CDW is driven by the delicate balance between magnetic energy savings and structural energy costs by Ge1 dimerization. Our findings broaden the study of intertwined electronic states in the magnetic kagome metal FeGe.

II. METHODS

A. Single-crystal growth, sample annealing, and characterization

The obtained as-grown single crystals of B35-type FeGe were synthesized using chemical vapor transport (CVT) [47]. Stoichiometric Fe (99.99%) and Ge powders (99.999%) and additional iodine as a transport agent were weighed and mixed. The precursors were loaded into a silicon quartz tube and sealed under high vacuum. The temperatures of the feedstock and crystallization regions were set at 600 °C and 550 °C, respectively, and kept for 2 weeks. The system was then naturally cooled to room temperature, and millimeter-sized FeGe single crystals were obtained in the middle of the quartz tube. The obtained as-grown single crystals were then sealed into quartz tubes under high vacuum and annealed at 320 °C. After being kept at 320 °C for 96 h, the tube was quickly taken out of the furnace and quenched in water [55,56]. Specific heat and resistivity measurements at ambient pressure were carried out in a Quantum Design physical property measurement system (PPMS-9T). Resistivity was measured by using a standard four-electrode method. Magnetic susceptibility measurements were performed using a Quantum Design superconducting quantum interference device magnetometer (MPMS-5 T).

B. High-pressure measurements

A piston cylinder cell (PCC) was used to generate hydrostatic pressure up to 2.38 GPa for high-pressure electrical resistivity measurements on S1. Electrical resistivity under pressure was measured with the standard four-probe method. Daphne 7373 was used as the pressure transmitting medium, and the pressure value in the PCC was estimated by the Sn superconducting transition temperature [57].

A palm-type cubic anvil cell (CAC) was used to generate hydrostatic pressure up to 14 GPa for high-pressure electrical resistivity measurements on S2. Three-axis compression together with the liquid pressure-transmitting medium glycerol can ensure excellent hydrostatic pressure environments in the CAC. Electrical resistivity under pressure was measured with the standard four-probe method. The pressure values inside the CAC at low temperature were estimated from the pressure-loading force calibration curve determined by measuring the superconducting transition temperature of lead (Pb) in CAC [58].

A diamond anvil cell (DAC) made from Be-Cu alloy was used to generate pressure exceeding 14 GPa for high-pressure electrical transport measurements. Two opposite diamond anvils with 300 μm culet and a c-BN gasket with a sample chamber with a diameter of 120 μm were used to generate pressure up to 48 and 29.8 GPa on S3 and S4, respectively. For S5, we used two opposite diamond anvils with a 500 μm culet and a 200 μm diameter sample chamber to generate pressure up to 15.2 GPa. Daphne 7373 was used as the pressure transmitting medium. We performed electrical transport measurements in a van der Pauw method using four Pt wires that were adhered to the FeGe samples. The pressure was applied and calibrated by using the ruby fluorescence shift [59] at room temperature. High-pressure electrical transport measurements were carried out in a refrigerator system (HelioxVT, Oxford Instruments).

High-pressure magnetic susceptibility measurements were performed in a miniature PCC using a superconducting quantum interference device (SQUID) magnetometer (MPMS-5 T, Quantum Design).

High-pressure synchrotron x-ray diffraction (XRD) was carried out at room temperature at beamline BL15U1 of the Shanghai synchrotron radiation facility (SSRF) with a

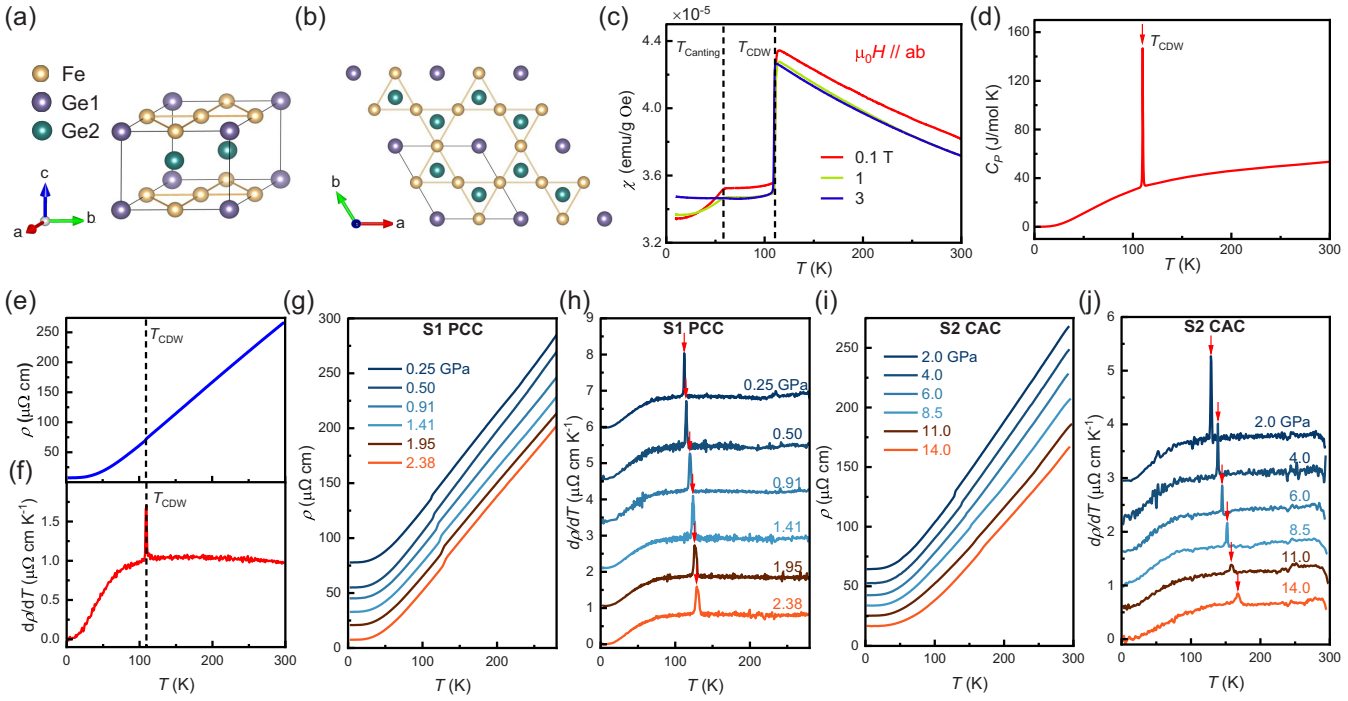

FIG. 1. (a) Pristine phase of B35-type FeGe crystallizes in a hexagonal structure with a space group of *P*6/*mmm*. Fe atoms (yellow balls) form two-dimensional kagome nets, with Ge1 atoms (purple balls) occupying the hexagonal centers where out-of-plane Ge2 atoms (cyan balls) form honeycomb lattices above and below the Fe triangular centers. (b) Top view of the crystal structure. (c) Temperature-dependent in-plane magnetic susceptibilities for a FeGe sample annealed at 320 °C measured under different applied magnetic fields. (d) Temperature-dependent specific heat data for the FeGe sample. A nearly divergent specific heat jump occurs near T_{CDW}, suggesting a typical first-order phase transition. (e), (f) Temperature-dependent in-plane resistivity and its derivative for the FeGe sample measured at ambient pressure. (g), (h) Temperature dependences of resistivity and its derivative for sample S1 measured in PCC under various pressures up to 2.38 GPa. (i), (j) Temperature dependences of resistivity and its derivative for sample S2 measured in CAC under various pressures up to 14 GPa. The curves in (g)–(j) were shifted vertically for clarity.

wavelength of $\lambda = 0.6199$ Å. A symmetric diamond anvil cell with a pair of 300 μm culet size anvils was used to generate pressure. A 110 μm diameter hole was drilled from the Re gasket as the sample chamber, and Daphne 7373 oil was loaded as a pressure transmitting medium. The pressure was calibrated by using ruby spectroscopy at room temperature. GSAS II [60] was used to refine the data using the Rietveld method.

C. DFT + *U* calculations

DFT + *U* calculations were performed using the Vienna *ab initio* simulation package (VASP) [61], with the generalized gradient approximation (GGA) of the Perdew-Burke-Ernzerhof variety [62] as the exchange-correlation potential. We apply the simplified approach introduced by Dudarev *et al.* (LDAUTYPE = 2) [63]. The lattice parameters *a* and *c* are relaxed in the non-CDW states by applying the desired pressure via the key word PSTRESS. The *A*-type AFM configuration is used in all the calculations. The internal atomic positions of the CDW superstructure are relaxed until the force is less than 0.001 eV/Å for each atom. The energy cutoff is set to 500 eV. Γ-centered *K*-point grids of $8 \times 8 \times 10$, $9 \times 9 \times 10$, and $9 \times 9 \times 3$ are used for the $2 \times 2 \times 2$, $\sqrt{3} \times \sqrt{3} \times 2$, and $\sqrt{3} \times \sqrt{3} \times 6$ CDW superstructures, respectively. The frozen phonon method combined with the PHONOPY package [64] is used to calculate the phonon spectra.

III. RESULTS AND DISCUSSION

The pristine phase of B35-type FeGe crystallizes in a hexagonal structure with a space group of *P*6/*mmm*. Each Fe_3Ge plane has a two-dimensional kagome net of Fe atoms, with Ge1 atoms occupying the hexagonal centers where out-of-plane Ge2 atoms form honeycomb lattices above and below the Fe triangular centers. The Fe_3Ge kagome layers and honeycomb Ge layers are stacked alternately along the *c* axis, as shown in Figs. 1(a) and 1(b). The CDW order in FeGe can be tuned by the annealing method. Neutron diffraction and scanning tunneling microscopy experiments revealed that the as-grown FeGe samples exhibit a short-range $2 \times 2 \times 2$ CDW with a typical coherence length of 2–4 nm [47,48,56], and no obvious anomalies at the CDW transition can be detected in resistivity measurements [47]. In contrast, a long-range $2 \times 2 \times 2$ CDW [55,56] was observed in the annealed samples, in which the correlation length is enhanced 10 times compared to the as-grown FeGe samples, along with a sharp specific heat jump and pronounced resistive kink appearing at the CDW transition temperature T_{CDW} [55,56,65]. Several XRD experiments have revealed that the superlattice reflections associated with the CDW order can be represented by three

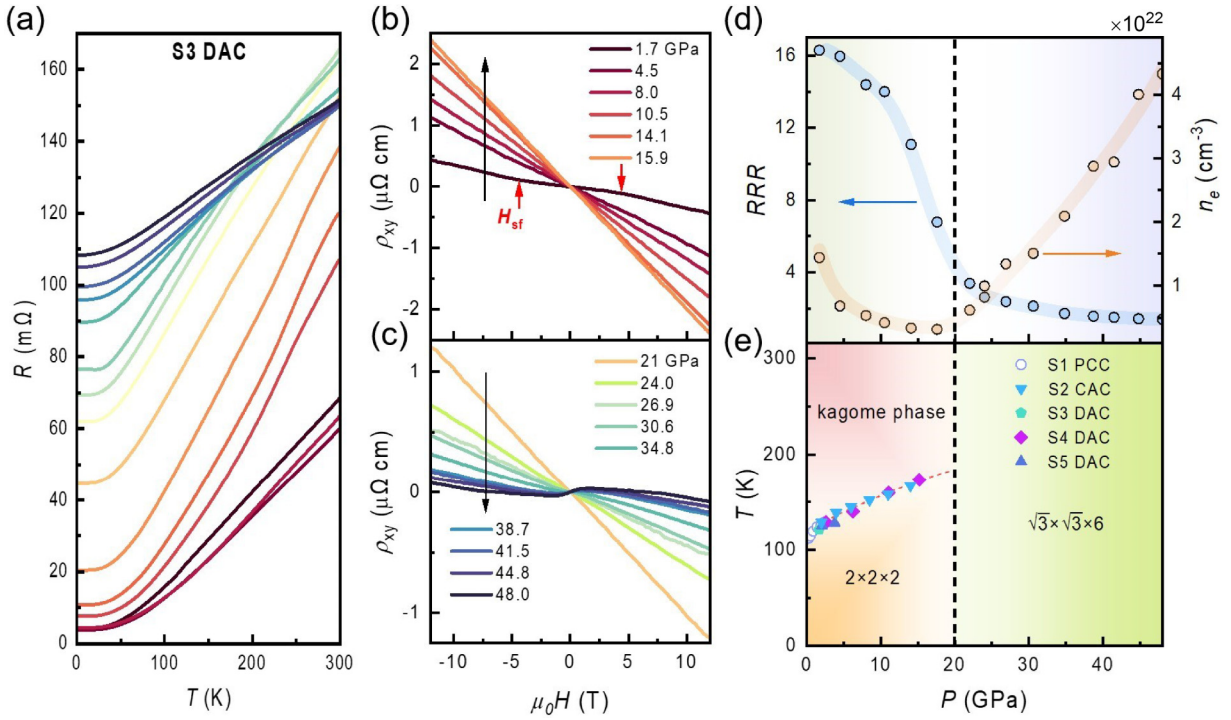

FIG. 2. (a) Temperature dependence of resistance under various pressures. (b), (c) Hall resistivity ρ_{xy} as a function of a magnetic field measured at 1.6 K under different pressures. (d) The evolution of RRR and carrier density n_e under pressure, which suggests that an anomalous transition appears at approximately 20 GPa. (e) Phase diagram with pressure for annealed FeGe.

independent **q**-vectors: (0.5, 0, 0), (–0.5, 0.5, 0), and (0, 0, 0.5) [47,49,65]. In order to facilitate the observation of CDW evolution under high pressure using resistivity measurements, we chose annealed samples with long-range CDW order for our experiments. We first checked the bulk physical properties of annealed FeGe at ambient pressure by using magnetization, heat capacity, and electrical transport measurements. Figure 1(c) shows the temperature-dependent in-plane magnetic susceptibilities under different applied magnetic fields for the FeGe sample. A sharp drop appears at approximately 110 K, indicating a long-range CDW transition [47]. In addition, a steplike feature near 60 K can be clearly observed, which corresponds to a change in the magnetic structure from a collinear *A*-type antiferromagnetic order to a double-cone antiferromagnetic structure [55]. This feature weakens with increasing magnetic field and becomes invisible at $\mu_0 H = 3$ T. As shown in Fig. S1 in the Supplemental Material [66] and Fig. 1(d), a hysteresis loop on the magnetic susceptibility and a nearly divergent specific heat jump can be observed near T_{CDW}, suggesting a typical first-order phase transition. The in-plane resistivity shows a monotonic drop with decreasing temperature and exhibits a distinct kinklike anomaly at T_{CDW}, as well as a sharp peak in the derivative of the resistivity, as shown in Figs. 1(e) and 1(f).

To investigate the evolution of the CDW state at high pressure, we systematically performed resistivity measurements on FeGe single crystals under pressure. Figures 1(g) and 1(h) show the temperature dependence of resistivity $\rho(T)$ and its derivative $\mathrm{d}\rho(T)/\mathrm{d}T$ of sample S1 measured with a piston cylinder cell (PCC) under various pressures up to 2.38 GPa. The kinklike anomaly in $\rho(T)$ due to the CDW transition and the corresponding sharp peak in $\mathrm{d}\rho(T)/\mathrm{d}T$ gradually move to higher temperatures with increasing pressure. By using a palm-type cubic anvil cell (CAC), higher-pressure resistance data were measured on sample S2 up to 14 GPa, which are shown in Fig. 1(i). The peak feature in $\mathrm{d}\rho(T)/\mathrm{d}T$ moves to higher temperatures and weakens gradually with increasing pressure, as shown in Fig. 1(f). In order to rule out that the weakening of this CDW transition and the increase of the residual resistivity ratio (RRR) may be caused by the gradual development of defects or disorders in the crystal with increasing pressure, we also measured the resistivity after decompressing to 5 GPa, which is shown in Fig. S3 [66]. We can clearly see that the peak in $\mathrm{d}\rho(T)/\mathrm{d}T$ due to the CDW transition recovers sharply after decompression, and the RRR value as well as the CDW transition temperature also match the values obtained from the compression process. These results suggest that the weakening of CDW with pressure is an intrinsic behavior of the sample and the CDW transition temperature can be increased from 110 K at ambient pressure to approximately 168 K around 14 GPa ($T_{\mathrm{CDW}} = 174$ K, $P = 15.2$ GPa for S4; see Fig. S5 [66]), which is strikingly different from that of other conventional CDW materials.

We also performed high-pressure electrical transport measurements on sample S3 up to 48 GPa, as shown in Fig. 2. Figure 2(a) displays the temperature dependence of the resistance under various pressures. The resistance exhibits metallic behavior over the entire pressure range from 1.7 to 48 GPa, and the residual resistivity increases with increasing pressure. We plot the residual resistivity ratio (RRR) as a function of pressure, as shown in Fig. 2(d). It can be clearly seen that RRR monotonically decreases when the pressure increases

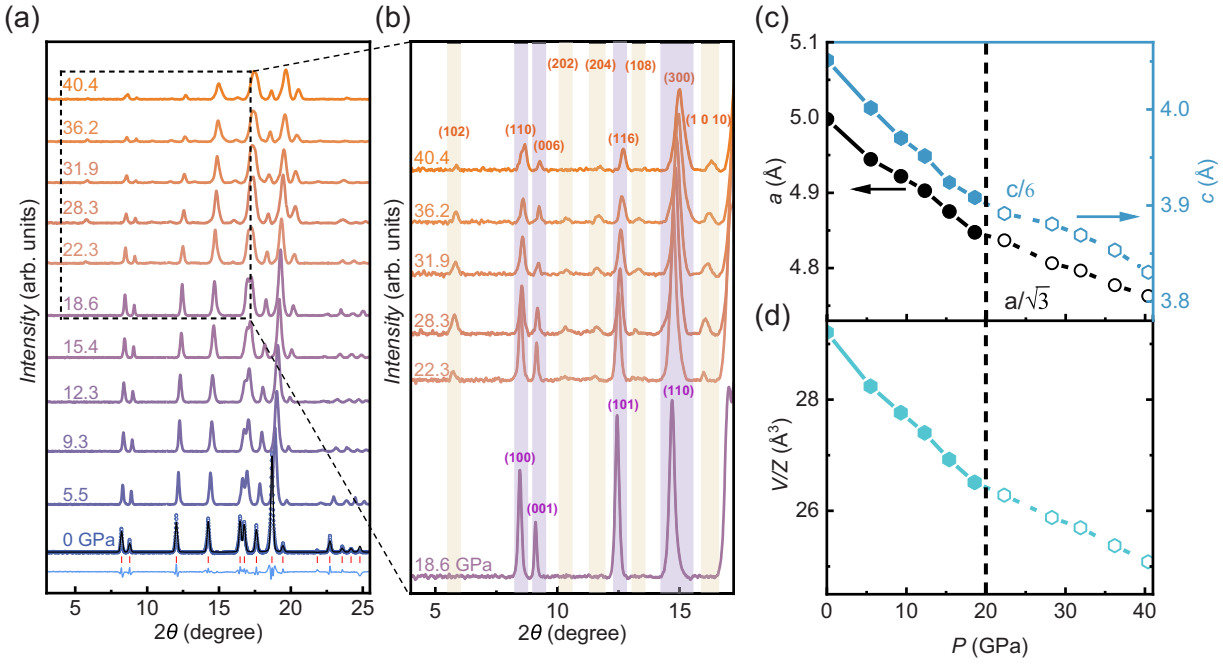

FIG. 3. (a) Powder XRD patterns of FeGe under various pressures up to 40.4 GPa. (b) Partial enlargement of the XRD patterns in the dashed box. All the peaks can be well indexed by using the $\sqrt{3} \times \sqrt{3} \times 6$ superlattice above 20 GPa. (c) Pressure dependence of the lattice parameters a and c. (d) Pressure dependence of the volume per formula unit (V/Z). For comparison with the low-pressure phase, a and c in the high-pressure phase are rescaled by $1/\sqrt{3}$ and 1/6, respectively. Weak slope changes are observed in a, c, and V/Z around 20 GPa.

and undergoes a slope change around 20 GPa. Such behavior is reproducible in sample S5, as shown in Fig. S8(c) [66]. Figures 2(b) and 2(c) display the Hall resistivity ρ_{xy} as a function of a magnetic field at different pressures measured at 1.6 K. At $P \sim 1.7$ GPa, ρ_{xy} shows linear behavior at a low magnetic field, and both the value and the slope of ρ_{xy} suddenly change at the spin-flop transition field H_{sf}, as indicated by the red arrows in Fig. 2(b), which is similar to the results at ambient pressure. The H_{sf} at 1.7 GPa is decreased to 4.4 T compared to 7 T at ambient pressure, yet the CDW transition temperature is increased.

As the pressure increases, ρ_{xy} becomes completely linear over the whole magnetic field range, and the slope increases with increasing pressure. Upon further increasing the pressure beyond 21 GPa, ρ_{xy} gradually deviates from the linear behavior, and the slope of the high-field ρ_{xy} gradually decreases with increasing pressure, as shown in Fig. 2(c). Low-field nonlinear behavior becomes progressively more pronounced with increasing pressure, as shown in Fig. S7 [66]. The derived pressure-dependent carrier density n_e is plotted in Fig. 2(d). The n_e first decreases with increasing pressure and then increases monotonically above 20 GPa. All of the above electrical transport results indicate that a phase transition may occur at approximately 20 GPa.

To further clarify the origin of the phase transition at approximately 20 GPa, we investigate the structural evolution at high pressure. We performed high-pressure x-ray diffraction (XRD) measurements on FeGe up to 40.4 GPa as shown in Fig. 3. The XRD patterns collected at different pressures are displayed in Fig. 3(a). The low-pressure XRD patterns can be well fitted using the hexagonal $P6/mmm$ space group of the ambient pressure structure, and selected Rietveld fitting results are shown in Figs. S9(a)–S9(c) [66]. When the pressure is increased above 20 GPa, new weak diffraction peaks appear in the XRD patterns. As shown in Fig. 3(b), all these observed peaks can be indexed very well using the $\sqrt{3} \times \sqrt{3} \times 6$ superlattice. The derived pressure dependence of the lattice parameters a, c and the volume per formula unit V/Z are shown in Figs. 3(c) and 3(d), respectively. We can observe a weak slope change in the normalized a, c and V/Z around 20 GPa, which corresponds to a possible CDW that appears at this pressure. These results indicate that a possible CDW with $\sqrt{3} \times \sqrt{3} \times 6$ spatial modulation appears at room temperature. Having collected all the data, we can map out the high-pressure phase diagram of FeGe, as shown in Fig. 2(e).

To clarify the origin of the unconventional T_{CDW} vs P behavior and pressure-induced possible CDW in FeGe, we performed theoretical calculations. Our DFT calculations are all based on the A-type magnetic configuration. Therefore, we first checked that the A-type AFM is still the most stable magnetic state under pressure in the Supplemental Material, Sec. VIII [66]. The lattice parameters a and c relaxed by DFT + U calculations at $U = 0.2$ eV under pressure are shown in Fig. S15 [66]. The calculated total energies, $E_{CDW} - E_{non\text{-}CDW}$, for various CDW states with respect to the non-CDW states, as functions of pressure P, are shown in Fig. 4(e). We consider four different CDW superstructures: (1) The $2 \times 2 \times 2$ CDW ground state with large dimerization of 1/4 Ge1 sites along the c axis at ambient pressure [Fig. 4(a)] [49,53]; (2) the $\sqrt{3} \times \sqrt{3} \times 2$ CDW superstructure with large dimerization of 1/3 of Ge1 sites [Fig. 4(b)] [53]; (3) the $\sqrt{3} \times \sqrt{3} \times 6$ CDW superstructure (space group P-6m2) with large dimerization of 1/3 of the Ge1 sites, but the in-plane coordinates of the dimerized Ge1-sites are (0, 0), (1/3, 1/3),

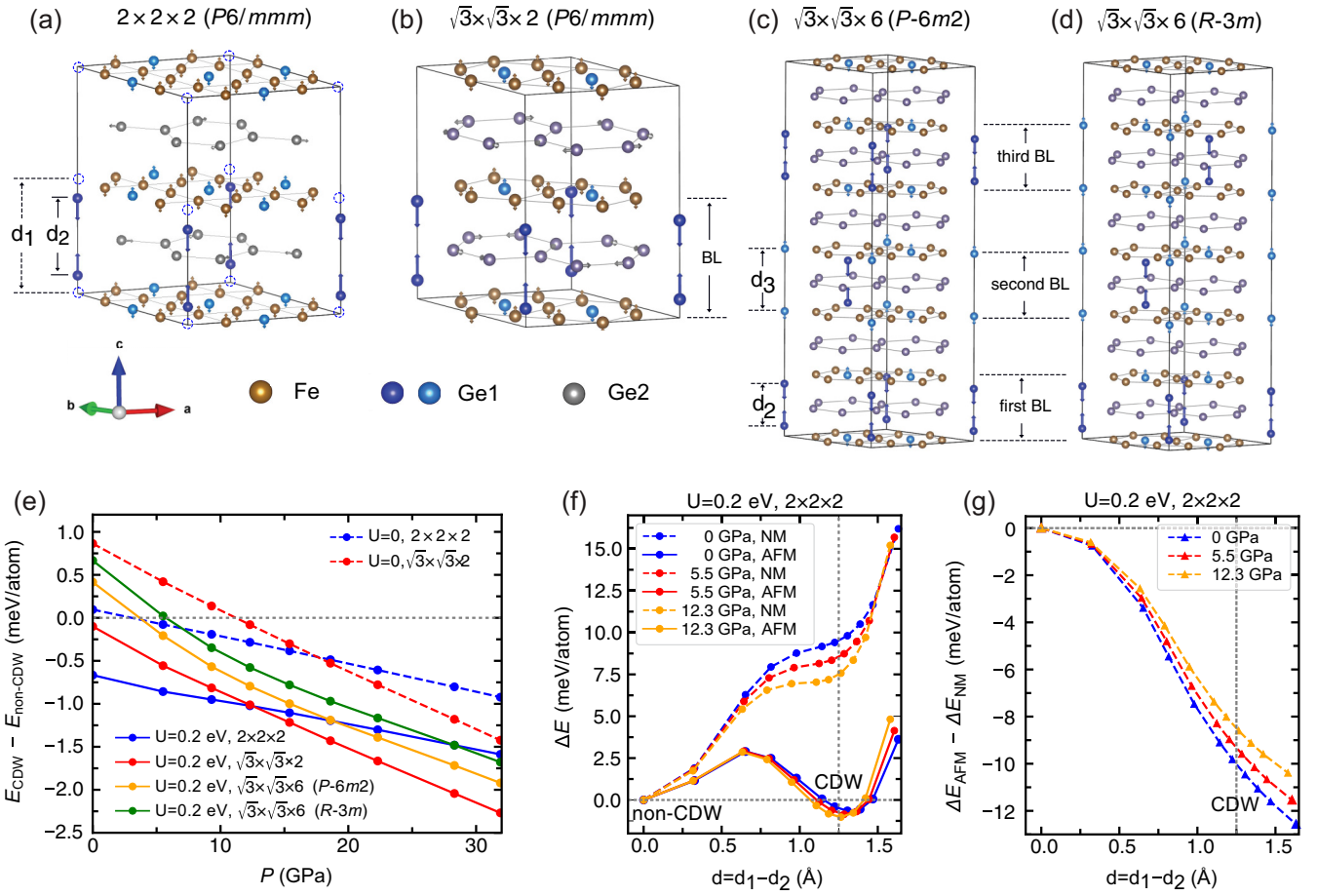

FIG. 4. (a) The $2 \times 2 \times 2$ CDW superstructure with a large dimerization of 1/4 of Ge1 sites (dark blue) along the c axis, where d_1 and d_2 are the Ge1-Ge1 bond lengths before and after Ge1 dimerization, respectively. The small distortions of other sites are illustrated by short arrows. (b) The $\sqrt{3} \times \sqrt{3} \times 2$ CDW superstructure with large dimerization of 1/3 of Ge1 sites, where "BL" means bilayer of kagome planes. (c), (d) Two possible $\sqrt{3} \times \sqrt{3} \times 6$ metastable CDW superstructures built on the $\sqrt{3} \times \sqrt{3} \times 2$ superstructure with different in-plane coordinates $(x,\ y)$ of the dimerized Ge1 sites (dark blue) in different bilayers. (0, 0), (1/3, 1/3), (0, 0) in (c), and (0,0), (1/3, 1/3), (2/3, 2/3) in (d) for the first, second, and third bilayers, respectively. The small distortions of other sites are not shown here. (e) The DFT + U calculated total energies, $E_{\text{CDW}} - E_{\text{non-CDW}}$, for various CDW superstructures with respect to the non-CDW states as functions of pressure. Dashed and solid curves are for $U = 0$ and $U = 0.2$ eV, respectively. (f) The total energies of the $2 \times 2 \times 2$ CDW superstructure, $\Delta E = E(d) - E(d = 0)$, as functions of the Ge1-dimerization strength $d = d_1 - d_2$ at $P = 0$, 5.5, 12.3 GPa, for nonmagnetic (NM) and antiferromagnetic (AFM) states, respectively. $d = 0$ means non-CDW state and the CDW states occur around $d = 1.25$ Å. (g) The energy difference of the AFM and NM states shown in (f), $\Delta E_{\text{AFM}} - \Delta E_{\text{NM}}$, as functions of Ge1-dimerization strength d, which measures the magnetic exchange energies.

(0, 0) for the first, second, and third bilayers of kagome planes [Fig. 4(c)]; (4) the $\sqrt{3} \times \sqrt{3} \times 6$ CDW superstructure (space group R-3m) with large dimerization of 1/3 of Ge1 sites, but the corresponding in-plane coordinates of the dimerized Ge1 sites are (0, 0), (1/3, 1/3), (2/3, 2/3) [Fig. 4(d)]. At $P = 0$ and $U = 0$, the $2 \times 2 \times 2$ CDW state is slightly higher in energy than the non-CDW state. It becomes the ground state after including a small $U \sim 0.2$ eV, which is reasonable since FeGe is a strongly correlated AFM metal and the spin polarization is sensitive to the U value. The key finding is that the total energies of the CDW states decrease with increasing pressure, indicating an increase in the CDW transition temperature, which agrees with our experimental observations. Remarkably, the $\sqrt{3} \times \sqrt{3} \times 2$ CDW superstructure becomes the ground state at higher pressure (> 12 GPa). We also found that $\sqrt{3} \times \sqrt{3} \times 6$ (P-6m2) and $\sqrt{3} \times \sqrt{3} \times 6$ (R-3m) become lower in energy than the $2 \times 2 \times 2$ CDW state at high pressure, indicating that they are metastable CDW states and could be stabilized under high pressure, which is consistent with our experimental observations. We use the P-6m2 space group to fit the XRD pattern measured at 36.2 GPa; all these observed peaks can be well fitted as shown in Fig. S9(d) [66]. It should be noted that the double-cone magnetic structure will not destroy the CDW state, and it only further reduces the symmetry of the CDW superstructure. Furthermore, the pressure-enhanced CDW state is very robust even in the presence of defects, as we discuss in the Supplemental Material, Sec. VIII [66].

CDW was also observed in other kagome metals. For instance, an exotic time-reversal symmetry breaking $2 \times 2 \times 2$ CDW has been discovered in AV_3Sb_5 (A = K, Rb, Cs) and is believed to originate from the nesting between VHSs near the Fermi level [17,19,21,23,24,27,67,68]. A $\sqrt{3} \times \sqrt{3}$ CDW was also observed in the kagome metal ScV_6Sn_6,

which is associated with strong electron-phonon couplings. Regardless of whether it originated from the nesting of VHSs or strong electron-phonon couplings [69–75], the CDW is rapidly suppressed with increasing pressure [37,38,76]. Our high-pressure electrical transport measurements revealed that the CDW in kagome magnet FeGe is gradually enhanced with increasing pressure, which is distinctly different from that of other CDW kagome materials. Since it is suggested that the nesting of VHSs at M points may play important roles in driving the CDW states in kagome systems, such as AV_3Sb_5 (A = K, Rb, Cs), we check how the VHSs in FeGe evolve under pressure. Figure S16 in the Suppplemental Material [66] shows the calculated band structures of the non-CDW states of FeGe at $U = 0.2$ eV for $P = 0$ and 9.3 GPa, respectively. We found that the VHS at the M point is further pushed away from the Fermi level under pressure, as shown in the dashed rectangle in Fig. S16 [66]. Considering that T_{CDW} is enhanced by pressure, this excludes the possibility of the nesting of VHSs as the CDW driver in FeGe. On the contrary, this result is consistent with the decrease in the total energies of the CDW state with increasing pressure obtained from our DFT + U calculations based on the large dimerization of Ge1 sites. Previous theoretical calculations proposed that the CDW driving force in FeGe is a delicate balance between magnetic energy savings and structural energy costs by Ge1 dimerization [53]. Applying pressure will affect both the structural and magnetic energies, which may further reduce the total energies of the CDW states. As shown by the dashed curves in Fig. 4(f), the energies of the nonmagnetic (NM) states decrease with increasing pressure at fixed Ge1-dimerization strength d (~ 1.25 Å), indicating it will cost less structural distortion energy by Ge1 dimerization in the lattice with a reduced c axis under pressure. Meanwhile, as shown in Fig. 4(g), the magnetic exchange energies increase with increasing pressure at fixed d (~ 1.25 Å), since the pressure tends to weaken the magnetism. This leads to less magnetic energy savings by Ge1 dimerization at high pressure. As shown by the solid curves in Fig. 4(f), the net effect is a further reduction of the total energy of the CDW state under pressure. Therefore, our experiments support such a scenario [53]. As shown in Fig. S17 [66], the phonon spectra of FeGe is still harmonically stable under high pressure, which indicates that the possible $\sqrt{3} \times \sqrt{3} \times 6$ CDW state is not primarily driven by electron-phonon coupling; instead, it is still driven by saving magnetic energy, same as the $2 \times 2 \times 2$ CDW state at ambient pressure.

Moreover, we found that the spin-flop transition field H_{sf} decreases with increasing pressure and is accompanied by an enhancement of CDW. The increase of CDW transition temperature under pressure is accompanied by the decrease of H_{sf}, which is similar to the variation of CDW transition temperature vs H_{sf} observed in different annealed samples at ambient pressure [55], and it can be well explained by the scenario mentioned above. The enhancement of CDW modulation under pressure leads to increased dimerization of Ge1 sites in the Fe_3Ge layers along the c axis, which weakens the spin anisotropy energy that aligns the c-axis moment, resulting in a decrease in H_{sf}.

Another key finding in this work is that the pressure-induced possible CDW emerges above 20 GPa, which agrees with the calculated metastable CDW states under high pressure. The pressure-induced CDW is rather rare. Previous experiments claim the pressure-induced CDW in the nonmagnetic material $SnSe_2$ [77] and 1T-VSe_2 [78], which is attributed to strong Fermi surface nesting or electron-phonon coupling. However, in our case, such CDW state is driven by magnetic energy savings, which also confirms that the various emergent CDW states in FeGe are driven by the delicate balance between magnetic energy savings and structural energy costs by Ge1 dimerization.

ACKNOWLEDGMENTS

This work is supported by the Innovation Program for Quantum Science and Technology (Grant No. 2021ZD0302802), the National Natural Science Foundation of China (Grant No. 11888101), the National Key Research and Development Program of the Ministry of Science and Technology of China (Grants No. 2019YFA0704900 and No. 2022YFA1602601), CAS Project for Young Scientists in Basic Research (Grant No. YBR-048), the Strategic Priority Research Program of the Chinese Academy of Sciences (Grant No. XDB25000000), Systematic Fundamental Research Program Leveraging Major Scientific and Technological Infrastructure, Chinese Academy of Sciences under Contract No. JZHKYPT-2021–08, and the Anhui Initiative in Quantum Information Technologies (Grant No. AHY160000). Y.W. was supported by the National Natural Science Foundation of China (Grant No. 12174365). X.W. and A.W. were supported by the National Natural Science Foundation of China (Grant No. 12004056), and the Chongqing Basic Research and Frontier Technology, China (Grant No. cstc2021jcyj-msxmX0661). J.Y. was also financially supported by the USTC Tang Scholar program. High-pressure synchrotron XRD work was performed at the BL15U1 beamline, Shanghai Synchrotron Radiation Facility (SSRF) in China. All the DFT + U calculations were performed on TianHe-1(A), the National Supercomputer Center in Tianjin, China. The high-pressure experiments were partially performed at the Cubic Anvil Cell (CAC) Station of Synergic Extreme Condition User Facility (SECUF).

[1] A. Mielke, Ferromagnetic ground-states for the hubbard-model on line graphs, J. Phys. A: Math. Gen. **24**, L73 (1991).

[2] A. Tanaka and H. Ueda, Stability of ferromagnetism in the Hubbard model on the kagome lattice, Phys. Rev. Lett. **90**, 067204 (2003).

[3] F. Pollmann, P. Fulde, and K. Shtengel, Kinetic ferromagnetism on a kagome lattice, Phys. Rev. Lett. **100**, 136404 (2008).

[4] H. M. Guo and M. Franz, Topological insulator on the kagome lattice, Phys. Rev. B **80**, 113102 (2009).

[5] M. L. Kiesel and R. Thomale, Sublattice interference in the kagome Hubbard model, Phys. Rev. B **86**, 121105(R) (2012).

[6] S. L. Yu and J. X. Li, Chiral superconducting phase and chiral spin-density-wave phase in a Hubbard model on the kagome lattice, Phys. Rev. B **85**, 144402 (2012).

[7] M. L. Kiesel, C. Platt, and R. Thomale, Unconventional Fermi surface instabilities in the kagome Hubbard model, Phys. Rev. Lett. **110**, 126405 (2013).

[8] T. Park, M. Ye, and L. Balents, Electronic instabilities of kagome metals: Saddle points and Landau theory, Phys. Rev. B **104**, 035142 (2021).

[9] M. G. Kang, L. D. Ye, S. Fang, J. S. You, A. Levitan, M. Y. Han, J. I. Facio, C. Jozwiak, A. Bostwick, E. Rotenberg, M. K. Chan, R. D. McDonald, D. Graf, K. Kaznatcheev, E. Vescovo, D. C. Bell, E. Kaxiras, J. van den Brink, M. Richter, M. P. Ghimire *et al.*, Dirac fermions and flat bands in the ideal kagome metal FeSn, Nat. Mater. **19**, 163 (2020).

[10] E. Tang, J. W. Mei, and X. G. Wen, High-temperature fractional quantum hall states, Phys. Rev. Lett. **106**, 236802 (2011).

[11] L. D. Ye, M. G. Kang, J. W. Liu, F. von Cube, C. R. Wicker, T. Suzuki, C. Jozwiak, A. Bostwick, E. Rotenberg, D. C. Bell, L. Fu, R. Comin, and J. G. Checkelsky, Massive Dirac fermions in a ferromagnetic kagome metal, Nature (London) **555**, 638 (2018).

[12] S. Okamoto, N. Mohanta, E. Dagotto, and D. N. Sheng, Topological flat bands in a kagome lattice multiorbital system, Commun. Phys. **5**, 198 (2022).

[13] W. S. Wang, Z. Z. Li, Y. Y. Xiang, and Q. H. Wang, Competing electronic orders on kagome lattices at Van Hove filling, Phys. Rev. B **87**, 115135 (2013).

[14] J. X. Yin, S. T. S. Zhang, H. Li, K. Jiang, G. Q. Chang, B. J. Zhang, B. Lian, C. Xiang, I. Belopolski, H. Zheng, T. A. Cochran, S. Y. Xu, G. Bian, K. Liu, T. R. Chang, H. Lin, Z. Y. Lu, Z. Q. Wang, S. Jia, W. H. Wang *et al.*, Giant and anisotropic many-body spin-orbit tunability in a strongly correlated kagome magnet, Nature (London) **562**, 91 (2018).

[15] G. Xu, B. Lian, and S. C. Zhang, Intrinsic quantum anomalous Hall effect in the kagome lattice $Cs_2LiMn_3F_{12}$, Phys. Rev. Lett. **115**, 186802 (2015).

[16] B. R. Ortiz, L. C. Gomes, J. R. Morey, M. Winiarski, M. Bordelon, J. S. Mangum, L. W. H. Oswald, J. A. Rodriguez-Rivera, J. R. Neilson, S. D. Wilson, E. Ertekin, T. M. McQueen, and E. S. Toberer, New kagome prototype materials: Discovery of KV_3Sb_5, RbV_3Sb_5, and CsV_3Sb_5, Phys. Rev. Mater. **3**, 094407 (2019).

[17] B. R. Ortiz, S. M. L. Teicher, Y. Hu, J. L. Zuo, P. M. Sarte, E. C. Schueller, A. M. Milinda Abeykoon, M. J. Krogstad, S. Rosenkranz, R. Osborn, R. Seshadri, L. Balents, J. He, and S. D. Wilson, CsV_3Sb_5: A Z_2 topological kagome metal with a superconducting ground state, Phys. Rev. Lett. **125**, 247002 (2020).

[18] H. Tan, Y. Liu, Z. Wang, and B. Yan, Charge density waves and electronic properties of superconducting kagome metals, Phys. Rev. Lett. **127**, 046401 (2021).

[19] H. Zhao, H. Li, B. R. Ortiz, S. M. L. Teicher, T. Park, M. X. Ye, Z. Q. Wang, L. Balents, S. D. Wilson, and I. Zeljkovic, Cascade of correlated electron states in the kagome superconductor CsV_3Sb_5, Nature (London) **599**, 216 (2021).

[20] W. Y. Duan, Z. Y. Nie, S. S. Luo, F. H. Yu, B. R. Ortiz, L. C. Yin, H. Su, F. Du, A. Wang, Y. Chen, X. Lu, J. J. Ying, S. D. Wilson, X. H. Chen, Y. Song, and H. Q. Yuan, Nodeless superconductivity in the kagome metal CsV_3Sb_5, Sci. China Phys. Mech. **64**, 107462 (2021).

[21] X. L. Feng, K. Jiang, Z. Q. Wang, and J. P. Hu, Chiral flux phase in the kagome superconductor AV_3Sb_5, Sci. Bull. **66**, 1384 (2021).

[22] H. X. Li, T. T. Zhang, T. Yilmaz, Y. Y. Pai, C. E. Marvinney, A. Said, Q. W. Yin, C. S. Gong, Z. J. Tu, E. Vescovo, C. S. Nelson, R. G. Moore, S. Murakami, H. C. Lei, H. N. Lee, B. J. Lawrie, and H. Miao, Observation of unconventional charge density wave without acoustic phonon anomaly in kagome superconductors AV_3Sb_5 (A = Rb, Cs), Phys. Rev. X **11**, 031050 (2021).

[23] C. Mielke, D. Das, J. X. Yin, H. Liu, R. Gupta, Y. X. Jiang, M. Medarde, X. Wu, H. C. Lei, J. Chang, P. Dai, Q. Si, H. Miao, R. Thomale, T. Neupert, Y. Shi, R. Khasanov, M. Z. Hasan, H. Luetkens, and Z. Guguchia, Time-reversal symmetry-breaking charge order in a kagome superconductor, Nature (London) **602**, 245 (2022).

[24] L. P. Nie, K. Sun, W. R. Ma, D. W. Song, L. X. Zheng, Z. W. Liang, P. Wu, F. H. Yu, J. Li, M. Shan, D. Zhao, S. J. Li, B. L. Kang, Z. M. Wu, Y. B. Zhou, K. Liu, Z. J. Xiang, J. J. Ying, Z. Y. Wang, T. Wu *et al.*, Charge-density-wave-driven electronic nematicity in a kagome superconductor, Nature (London) **604**, 59 (2022).

[25] D. W. Song, L. X. Zheng, F. H. Yu, J. Li, L. P. Nie, M. Shan, D. Zhao, S. J. Li, B. L. Kang, Z. M. Wu, Y. B. Zhou, K. L. Sun, K. Liu, X. G. Luo, Z. Y. Wang, J. J. Ying, X. G. Wan, T. Wu, and X. H. Chen, Orbital ordering and fluctuations in a kagome superconductor CsV_3Sb_5, Sci. China Phys. Mech. **65**, 247462 (2022).

[26] B. R. Ortiz, S. M. L. Teicher, L. Kautzsch, P. M. Sarte, N. Ratcliff, J. Harter, J. P. C. Ruff, R. Seshadri, and S. D. Wilson, Fermi surface mapping and the nature of charge-density-wave order in the kagome superconductor CsV_3Sb_5, Phys. Rev. X **11**, 041030 (2021).

[27] Y. X. Jiang, J. X. Yin, M. M. Denner, N. Shumiya, B. R. Ortiz, G. Xu, Z. Guguchia, J. Y. He, M. S. Hossain, X. X. Liu, J. Ruff, L. Kautzsch, S. T. S. Zhang, G. Q. Chang, I. Belopolski, Q. Zhang, T. A. Cochran, D. Multer, M. Litskevich, Z. J. Cheng *et al.*, Unconventional chiral charge order in kagome superconductor KV_3Sb_5, Nat. Mater. **20**, 1353 (2021).

[28] F. H. Yu, T. Wu, Z. Y. Wang, B. Lei, W. Z. Zhuo, J. J. Ying, and X. H. Chen, Concurrence of anomalous Hall effect and charge density wave in a superconducting topological kagome metal, Phys. Rev. B **104**, L041103 (2021).

[29] C. Y. Guo, C. Putzke, S. Konyzheva, X. W. Huang, M. Gutierrez-Amigo, I. Errea, D. Chen, M. G. Vergniory, C. Felser, M. H. Fischer, T. Neupert, and P. J. W. Moll, Switchable chiral transport in charge-ordered kagome metal CsV_3Sb_5, Nature (London) **611**, 461 (2022).

[30] H. Li, H. Zhao, B. R. Ortiz, T. Park, M. X. Ye, L. Balents, Z. Q. Wang, S. D. Wilson, and I. Zeljkovic, Rotation symmetry breaking in the normal state of a kagome superconductor KV_3Sb_5, Nat. Phys. **18**, 265 (2022).

[31] Y. G. Zhong, J. J. Liu, X. X. Wu, Z. Guguchia, J. X. Yin, A. Mine, Y. K. Li, S. Najafzadeh, D. Das, C. Mielke, R. Khasanov, H. Luetkens, T. Suzuki, K. C. Liu, X. L. Han, T. Kondo, J. P. Hu, S. Shin, Z. W. Wang, X. Shi *et al.*, Nodeless electron pairing

in CsV_3Sb_5-derived kagome superconductors, Nature (London) **617**, 488 (2023).

[32] M. G. Kang, S. A. Fang, J. K. Kim, B. R. Ortiz, S. H. Ryu, J. M. Kim, J. Yoo, G. Sangiovanni, D. Di Sante, B. G. Park, C. Jozwiak, A. Bostwick, E. Rotenberg, E. Kaxiras, S. D. Wilson, J. H. Park, and R. Comin, Twofold Van Hove singularity and origin of charge order in topological kagome superconductor CsV_3Sb_5, Nat. Phys. **18**, 301 (2022).

[33] X. K. Wen, F. H. Yu, Z. G. Gui, Y. Q. Zhang, X. Y. Hou, L. Shan, T. Wu, Z. J. Xiang, Z. Y. Wang, J. J. Ying, and X. H. Chen, Emergent superconducting fluctuations in compressed kagome superconductor CsV_3Sb_5, Sci. Bull. **68**, 259 (2023).

[34] Z. Y. Shan, P. K. Biswas, S. K. Ghosh, T. Tula, A. D. Hillier, D. Adroja, S. Cottrell, G. H. Cao, Y. Liu, X. F. Xu, Y. Song, H. Q. Yuan, and M. Smidman, Muon spin relaxation study of the layered kagome superconductor CsV_3Sb_5, Phys. Rev. Res. **4**, 033145 (2022).

[35] S. Y. Yang, Y. J. Wang, B. R. Ortiz, D. F. Liu, J. Gayles, E. Derunova, R. Gonzalez-Hernandez, L. Smejkal, Y. L. Chen, S. S. P. Parkin, S. D. Wilson, E. S. Toberer, T. McQueen, and M. N. Ali, Giant, unconventional anomalous Hall effect in the metallic frustrated magnet candidate, KV_3Sb_5, Sci. Adv. **6**, eabb6003 (2020).

[36] M. M. Denner, R. Thomale, and T. Neupert, Analysis of charge order in the kagome metal AV_3Sb_5 (A = K, Rb, Cs), Phys. Rev. Lett. **127**, 217601 (2021); **128**, 099901(E) (2022).

[37] F. H. Yu, D. H. Ma, W. Z. Zhuo, S. Q. Liu, X. K. Wen, B. Lei, J. J. Ying, and X. H. Chen, Unusual competition of superconductivity and charge-density-wave state in a compressed topological kagome metal, Nat. Commun. **12**, 3645 (2021).

[38] K. Y. Chen, N. N. Wang, Q. W. Yin, Y. H. Gu, K. Jiang, Z. J. Tu, C. S. Gong, Y. Uwatoko, J. P. Sun, H. C. Lei, J. P. Hu, and J.-G. Cheng, Double superconducting dome and triple enhancement of T_c in the kagome superconductor CsV_3Sb_5 under high pressure, Phys. Rev. Lett. **126**, 247001 (2021).

[39] X. K. Teng, J. S. Oh, H. X. Tan, L. B. Chen, J. W. Huang, B. Gao, J. X. Yin, J. H. Chu, M. Hashimoto, D. H. Lu, C. Jozwiak, A. Bostwick, E. Rotenberg, G. E. Granroth, B. H. Yan, R. J. Birgeneau, P. C. Dai, and M. Yi, Magnetism and charge density wave order in kagome FeGe, Nat. Phys. **19**, 814 (2023).

[40] T. Ohoyama, K. Yasukochi, and K. Kanematsu, A new intermetallic compound FeGe, J. Phys. Soc. Jpn. **18**, 589 (1963).

[41] O. Beckman, K. Carrander, L. Lundgren, and M. Richardson, Susceptibility measurements and magnetic ordering of hexagonal FeGe, Phys. Scr. **6**, 151 (1972).

[42] L. Haggstrom, T. Ericsson, R. Wappling, and E. Karlsson, Mossbauer study of hexagonal FeGe, Phys. Scr. **11**, 55 (1975).

[43] U. Gafvert, L. Lundgren, B. Westerstrandh, and O. Beckman, Crystalline anisotropy energy of uniaxial antiferromagnets evaluated from low field torque data, J. Phys. Chem. Solids **38**, 1333 (1977).

[44] B. Lebech, J. Bernhard, and O. Beckman, The low-temperature magnetic-structure of hexagonal FeGe, Acta Crystallogr., Sect. A **40**, C260 (1984).

[45] J. Bernhard, B. Lebech, and O. Beckman, Neutron-diffraction studies of the low-temperature magnetic-structure of hexagonal FeGe, Acta Crystallogr., Sect. A **14**, 2379 (1984).

[46] J. Bernhard, B. Lebech, and O. Beckman, Magnetic phase-diagram of hexagonal fege determined by neutron-diffraction, Acta Crystallogr., Sect. A **18**, 539 (1988).

[47] X. K. Teng, L. B. Chen, F. Ye, E. Rosenberg, Z. Y. Liu, J. X. Yin, Y. X. Jiang, J. S. Oh, M. Z. Hasan, K. J. Neubauer, B. Gao, Y. F. Xie, M. Hashimoto, D. H. Lu, C. Jozwiak, A. Bostwick, E. Rotenberg, R. J. Birgeneau, J. H. Chu, M. Yi *et al.*, Discovery of charge density wave in a kagome lattice antiferromagnet, Nature (London) **609**, 490 (2022).

[48] J. X. Yin, Y. X. Jiang, X. Teng, M. S. Hossain, S. Mardanya, T. R. Chang, Z. Ye, G. Xu, M. M. Denner, T. Neupert, B. Lienhard, H. B. Deng, C. Setty, Q. Si, G. Chang, Z. Guguchia, B. Gao, N. Shumiya, Q. Zhang, T. A. Cochran *et al.*, Discovery of charge order and corresponding edge state in kagome magnet FeGe, Phys. Rev. Lett. **129**, 166401 (2022).

[49] H. Miao, T. T. Zhang, H. X. Li, G. Fabbris, A. H. Said, R. Tartaglia, T. Yilmaz, E. Vescovo, J. X. Yin, S. Murakami, X. L. Feng, K. Jiang, X. L. Wu, A. F. Wang, S. Okamoto, Y. L. Wang, and H. N. Lee, Signature of spin-phonon coupling driven charge density wave in a kagome magnet, Nat. Commun. **14**, 6183 (2023).

[50] S. Shao, J. X. Yin, I. Belopolski, J. Y. You, T. Hou, H. Y. Chen, Y. X. Jiang, M. S. Hossain, M. Yahyavi, C. H. Hsu, Y. P. Feng, A. Bansil, M. Z. Hasan, and G. Q. Chang, Intertwining of magnetism and charge ordering in kagome FeGe, ACS Nano **17**, 10164 (2023).

[51] L. Wu, Y. T. Hu, D. Wang, and X. G. Wan, Electron correlation-induced charge density wave in FeGe, Chin. Phys. Lett. **40**, 117103 (2023).

[52] H.-Y. Ma, J.-X. Yin, M. Z. Hasan, and J. P. Liu, Theory for charge density wave and orbital-flux state in antiferromagnetic kagome, Chin. Phys. Lett. **41**, 047103 (2024).

[53] Y. L. Wang, Enhanced spin-polarization via partial Ge-dimerization as the driving force of the $2 \times 2 \times 2$ CDW in FeGe, Phys. Rev. Mater. **7**, 104006 (2023).

[54] B. H. Zhang, J. Y. Ji, C. S. Xu, and H. J. Xiang, Triple-well charge density wave transition driven by partially occupied Ge electronic states in kagome FeGe, arXiv:2307.10565v1.

[55] X. L. Wu, X. R. Mi, L. Zhang, C.-W. Wang, N. Maraytta, X. Y. Zhou, M. Q. He, M. Merz, Y. S. Chai, and A. F. Wang, Annealing tunable charge density wave order in a magnetic kagome material FeGe, Phys. Rev. Lett. **132**, 256501 (2024).

[56] Z. Y. Chen, X. L. Wu, S. M. Zhou, J. K. Zhang, R. T. Yin, Y. J. Li, M. Z. Li, J. S. Gong, M. Q. He, Y. S. Chai, X. Y. Zhou, Y. l. Wang, A. F. Wang, Y.-J. Yan, and D.-L. Feng, Long-ranged charge order conspired by magnetism and lattice in an antiferromagnetic kagome metal, arXiv:2307.07990.

[57] L. D. Jennings and C. A. Swenson, Effects of pressure on the superconducting transition temperatures of Sn, In, Ta, Tl, and Hg, Phys. Rev. **112**, 31 (1958).

[58] J. G. Cheng, K. Matsubayashi, S. Nagasaki, A. Hisada, T. Hirayama, M. Hedo, H. Kagi, and Y. Uwatoko, Integrated-fin gasket for palm cubic-anvil high pressure apparatus, Rev. Sci. Instrum. **85**, 093907 (2014).

[59] H. K. Mao, J. Xu, and P. M. Bell, Calibration of the ruby pressure gauge to 800-kbar under quasi-hydrostatic conditions, J. Geophys. Res.: Solid Earth **91**, 4673 (1986).

[60] B. H. Toby and R. B. Von Dreele, GSAS-II: The genesis of a modern open-source all purpose crystallography software package, J. Appl. Crystallogr. **46**, 544 (2013).

[61] G. Kresse and J. Furthmuller, Efficient iterative schemes for *ab initio* total-energy calculations using a plane-wave basis set, Phys. Rev. B **54**, 11169 (1996).

[62] J. P. Perdew, K. Burke, and M. Ernzerhof, Generalized gradient approximation made simple, Phys. Rev. Lett. **77**, 3865 (1996).

[63] S. L. Dudarev, G. A. Botton, S. Y. Savrasov, C. J. Humphreys, and A. P. Sutton, Electron-energy-loss spectra and the structural stability of nickel oxide: An LSDA+U study, Phys. Rev. B **57**, 1505 (1998).

[64] A. Togo and I. Tanaka, First principles phonon calculations in materials science, Scr. Mater. **108**, 1 (2015).

[65] C. F. Shi, Y. Liu, B. B. Maity, Q. Wang, S. R. Kotla, S. Ramakrishnan, C. Eisele, H. Agarwal, L. Noohinejad, Q. Tao, B. J. Kang, Z. F. Lou, X. H. Yang, Y. P. Qi, X. Lin, Z.-A. Xu, A. Thamizhavel, G.-H. Cao, S. Smaalen, S. X. Cao *et al.*, Disordered structure for long-range charge density wave order in annealed crystals of magnetic kagome FeGe, arXiv:2308.09034.

[66] See Supplemental Material at http://link.aps.org/supplemental/10.1103/PhysRevResearch.6.033222 for further details on the experimental methods and DFT calculations, and which includes Refs. [54,56].

[67] H. Chen, H. T. Yang, B. Hu, Z. Zhao, J. Yuan, Y. Q. Xing, G. J. Qian, Z. H. Huang, G. Li, Y. H. Ye, S. Ma, S. L. Ni, H. Zhang, Q. W. Yin, C. S. Gong, Z. J. Tu, H. C. Lei, H. X. Tan, S. Zhou, C. M. Shen *et al.*, Roton pair density wave in a strong-coupling kagome superconductor, Nature (London) **599**, 222 (2021).

[68] Z. W. Liang, X. Y. Hou, F. Zhang, W. R. Ma, P. Wu, Z. Y. Zhang, F. H. Yu, J. J. Ying, K. Jiang, L. Shan, Z. Y. Wang, and X. H. Chen, Three-dimensional charge density wave and surface dependent vortex core states in a kagome superconductor CsV_3Sb_5, Phys. Rev. X **11**, 031026 (2021).

[69] Hasitha W. Suriya Arachchige, W. R. Meier, M. Marshall, T. Matsuoka, R. Xue, M. A. McGuire, R. P. Hermann, H. Cao, and D. Mandrus, Charge density wave in kagome lattice intermetallic ScV_6Sn_6, Phys. Rev. Lett. **129**, 216402 (2022).

[70] H. X. Tan and B. H. Yan, Abundant lattice instability in kagome metal ScV_6Sn_6, Phys. Rev. Lett. **130**, 266402 (2023).

[71] A. Korshunov, H. Hu, D. Subires, Y. Jiang, D. Călugăru, X. Feng, A. Rajapitamahuni, C. Yi, S. Roychowdhury, M. G. Vergniory, J. Strempfer, C. Shekhar, E. Vescovo, D. Chernyshov, A. H. Said, A. Bosak, C. Felser, B. A. Bernevig, and S. Blanco-Canosa, Softening of a flat phonon mode in the kagome ScV_6Sn_6, Nat. Commun. **14**, 6646 (2023).

[72] T. C. Hu, H. Q. Pi, S. X. Xu, L. Yue, Q. Wu, Q. M. Liu, S. J. Zhang, R. S. Li, X. Y. Zhou, J. Y. Yuan, D. Wu, T. Dong, H. M. Weng, and N. L. Wang, Optical spectroscopy and band structure calculations of the structural phase transition in the vanadium-based kagome metal ScV_6Sn_6, Phys. Rev. B **107**, 165119 (2023).

[73] S. Z. Cao, C. C. Xu, H. Fukui, T. Manjo, Y. Dong, M. Shi, Y. Liu, C. Cao, and Y. Song, Competing charge-density wave instabilities in the kagome metal ScV_6Sn_6, Nat. Commun. **14**, 7671 (2023).

[74] S. Y. Lee, C. Won, J. Kim, J. Yoo, S. Park, J. Denlinger, C. Jozwiak, A. Bostwick, E. Rotenberg, R. Comin, M. Kang, and J.-H. Park, Nature of charge density wave in kagome metal ScV_6Sn_6, npj Quantum Mater. **9**, 15 (2024).

[75] Y. Hu, J. Z. Ma, Y. X. Li, Y. Jiang, D. J. Gawryluk, T. C. Hu, J. Teyssier, V. Multian, Z. Y. Yin, S. Xu, S. Shin, I. Plokhikh, X. l. Han, N. C. Plumb, Y. Liu, J.-X. Yin, Z. Guguchia, Y. Zhao, A. P. Schnyder, X. X. Wu *et al.*, Phonon promoted charge density wave in topological kagome metal ScV_6Sn_6, Nat. Commun. **15**, 1658 (2024).

[76] X. X. Zhang, J. Hou, W. Xia, Z. Xu, P. T. Yang, A. Q. Wang, Z. Y. Liu, J. Shen, H. Zhang, X. L. Dong, Y. Uwatoko, J. P. Sun, B. S. Wang, Y. F. Guo, and J. G. Cheng, Destabilization of the charge density wave and the absence of superconductivity in ScV_6Sn_6 under high pressures up to 11 GPa, Materials **15**, 7372 (2022).

[77] J. J. Ying, H. Paudyal, C. Heil, X. J. Chen, V. V. Struzhkin, and E. R. Margine, Unusual pressure-induced periodic lattice distortion in $SnSe_2$, Phys. Rev. Lett. **121**, 027003 (2018).

[78] R. Sereika, C. Park, C. Kenney-Benson, S. Bandaru, N. J. English, Q. W. Yin, H. C. Lei, N. Chen, C. J. Sun, S. M. Heald, J. C. Ren, J. Chang, Y. Ding, and H. K. Mao, Novel superstructure-phase two-dimensional material 1T-VSe_2 at high pressure, J. Phys. Chem. Lett. **11**, 380 (2020).